Hole and Electron Effective Masses in Single InP Nanowires With a Wurtzite-Zincblende Homojunction

D. Tedeschi,[1] H. A. Fonseka,[2,3] E. Blundo,[1] A. Granados del Águila,[4] Y. Guo[2,#], H. H. Tan,[2,5] P. C. M. Christianen,[6] C. Jagadish,[2,5] A.Polimeni[1,] and M. De Luca[7,*]*

[1]Dipartimento di Fisica, Sapienza Università di Roma, Piazzale A. Moro 2, 00185 Roma, Italy

[2]Department of Electronic Materials Engineering, Research School of Physics, The Australian National University, Canberra, ACT 2601, Australia

[3]Department of Physics, University of Warwick, Coventry CV4 7AL, United Kingdom

[4]Division of Physics and Applied Physics, School of Physical and Mathematical Sciences, Nanyang Technological University, Singapore 637371, Singapore

[5]ARC Centre of Excellence for Transformative Meta-Optical Systems, Research School of Physics, The Australian National University, Canberra, ACT 2601, Australia

[6]High Field Magnet Laboratory (HFML – EMFL), Radboud University, Toernooiveld 7, NL-6525 ED Nijmegen, The Netherlands

[7]Department of Physics, University of Basel, Klingelbergstrasse 82, 4056 Basel, Switzerland

ABSTRACT. The formation of wurtzite (WZ) phase in III-V nanowires (NWs) such as GaAs and InP is a complication hindering the growth of pure-phase NWs, but it can also be exploited to form NW homostructures consisting of alternate zincblende (ZB) and WZ segments. This leads to different forms of nanostructures, such as crystal-phase superlattices and quantum dots. Here we investigate the electronic properties of the simplest, yet challenging, of such homostructures: InP NWs with a single homojunction between pure ZB and WZ segments. Polarization-resolved micro-photoluminescence (μ-PL) measurements on single NWs provide a tool to gain insights into the interplay between NW geometry and crystal phase. We also exploit this homostructure to simultaneously measure effective masses of charge carriers and excitons in ZB and WZ InP NWs, reliably. Magneto-μ-PL measurements carried out on individual NWs up to 29 T at 77 K allow us to determine the free exciton reduced masses of the ZB and WZ crystal phases, showing the heavier character of that of the WZ phase, and to deduce the effective mass of electrons in ZB InP NWs ($m^e = 0.080\, m_0$). Finally, we obtain the reduced mass of light-hole excitons in WZ InP by probing the second optically permitted transition $\Gamma_7^{\mathrm{C}} \leftrightarrow \Gamma_{7\mathrm{u}}^{\mathrm{V}}$ with magneto-μ-PL measurements carried out at room temperature. This information is used to extract the experimental light-hole effective mass in WZ InP, which is found to be $m^{lh} = 0.26\, m_0$, a value much smaller than the one of the heavy hole mass. Besides being a valuable test for band structure calculations, the knowledge of carrier masses in WZ and ZB InP is important in view of the optimization of the efficiency of solar cells, which is one of the main applications of InP NWs.

KEYWORDS Wurtzite and zincblende, InP nanowires, crystal-phase homostructures, excitons, magneto-photoluminescence, carrier effective mass, light hole

One of the most striking characteristics of nanowires (NWs) is the possibility to obtain non-nitride III-V semiconductors in the wurtzite (WZ) crystal phase in addition to the zincblende (ZB) phase, which is the stable bulk form. This has enriched the possibility of modulating the physical properties of NWs with novel types of structures, in which ZB and WZ segments are juxtaposed[1]. Such homostructures (*i.e.*, same composition, different crystal phase) have allowed to circumvent two main problems related to conventional heterojunctions formed between two different materials; namely interface mixing and lattice mismatch, leading to atomically sharp, unstrained junctions. This characteristic has opened the door to crystal-phase engineering with NWs[1,2,3,4]. Besides the control over crystal phase and composition, the in depth understanding of the growth processes and constant improvements in epitaxial growth techniques have enabled the growth of NWs in various geometrical shapes, for example those with a kink[5,6,7,8], namely a change in growth direction. This peculiar characteristic of NWs has enabled a wide range of applications, especially as bioprobes[7,8]. Homo-structured NWs can also be grown with[9,10] or without[1,2,4,11,12] a kinking, in a controlled manner.

Despite the vast amount of literature available on the growth and structural characterization of NW homostructures, there are only few reports on their optical properties[2,10,11,12], retarding their utilization in NW devices. The limited progress in understanding and exploiting the optical properties of crystal-phase homostructures is primarily due to the ambiguity regarding even some of the basic parameters of the WZ crystal structure, such as the band gap energy and the symmetry group of the topmost valence band and the lowest conduction band. This is still the case for GaAs[13,14] and GaP[15,16]. Recently, the definitive band gap energies of InP[17] and InAs[18,19] WZ NWs were ascertained. However, there is only limited investigation on the carrier mass and gyromagnetic factor values of non-nitrides WZ NWs[20,21,22,23,24,25,26] —which are different from ZB

and thus unknown, despite being extremely important for engineering WZ NW devices, where the transport and spin properties play a crucial role.

Knowledge of the carrier mass in WZ and ZB InP NWs is important in many aspects. First, it is a valuable test for band structure calculations, useful especially for the less known WZ crystal structure. In particular, in III-V WZ NWs the structure of the valence bands stems from degenerate *p*-like states that split *via* the spin-orbit coupling and the crystal field[27], and the hole effective mass values quantitatively reflect the extent of such fundamental interactions. In addition to this fundamental importance, the knowledge of carrier masses in NWs has technological implications. For instance, the hole effective masses significantly influence the efficiency of solar cells[28], which is one of the main applications of InP NWs[29]. Indeed, in WZ InP the heavy- and light-hole effective masses (pertaining to the A and B bands, respectively) determine the density of states and hence the NW photon absorption up to about 1.6 eV at room temperature[17], which corresponds to an important infrared portion of the solar spectrum. Furthermore, the hole mass affects the mobility as well as other parameters that rule the efficiency of a photovoltaic devices like the open-circuit voltage[28].

Optical properties, such as band gap energy, and magneto-optical properties, such as carrier mass and gyromagnetic factor, can be investigated by photoluminescence (PL), PL excitation and magneto-PL. Most of the fundamental electronic properties of WZ GaP[15,16], GaAs[14,23], InP[20,30,31], and InGaAs[32,33] NWs have been investigated using a combination of these experimental techniques. Moreover, μ-PL gives the opportunity to study individual NWs, thus enabling a correlation between the specific physical properties of a given NW with its structural characteristics[14]. Here we report μ-PL and magneto-μ-PL studies of a homostructure kinked InP NW containing two separate segments of defect-free ZB and WZ crystal phases. We exploit the

presence of two crystal phases in a same NW and their good optical quality to assess some crucial transport parameters, such as the electron and hole effective masses of WZ and ZB InP NWs. This is enabled by the possibility to carry out magneto-PL measurements on both crystal phases simultaneously and still separately identify PL signals (due to very different ZB and WZ emission energies). Initial polarization-resolved μ-PL measurements on single NWs highlight the different selection rules between ZB and WZ sections with a degree of polarization of 50 % in WZ and -25 % in ZB. A kink angle of ~ 16° between the two segments is also determined by polarization-resolved μ-PL measurements.

By magneto-μ-PL measurements carried out at 77 K, we determine the band-gap exciton masses of ZB and WZ InP simultaneously. This allows for a direct comparison between the masses of the two crystal phases, without the need to assume for ZB InP the values of the bulk. Furthermore, using the impurity-related recombination from the ZB segment, we determine in NWs the electron effective mass of ZB InP, which has been only known for bulk. We find it to be equal to 0.080 m_0, similar to the bulk value. Finally, we performed μ-PL measurements at room temperature on single NWs under very high magnetic fields (29 T). Using this combination of challenging experimental conditions that has not been realized before, we assess for the first time the mass of excitons involved in the second optically allowed transition $\Gamma_7^{\mathrm{C}} \leftrightarrow \Gamma_{7\mathrm{u}}^{\mathrm{V}}$, namely the B band, in WZ InP. Then, we determine the light-hole effective mass pertinent to the $\Gamma_{7\mathrm{u}}^{\mathrm{V}}$ valence band in a plane containing the $\hat{c}$ axis to be equal to $m^{lh} = 0.26 \pm 0.05\, m_0$, in excellent agreement with the recent theoretical calculations[34]. We also extract the mass of excitons involved in the A band and of the heavy holes at RT, and compare these values to the low-temperature values.

Results and discussion

Synthesis of the samples. The kinked InP NWs were synthesized by vapor-liquid-solid mechanism on InP (100) substrates using Au particles with diameters of 30 nm. More details on the growth conditions can be found in ref. 9 and in the methods section. Here we stress that after growing for approximately 90 minutes (estimation based on the growth rate: ~1 μm per hour), the [100] NWs kink to a <111> orientation by forming an inclined twin[9]. It should be noted that this spontaneous change in growth direction takes place without any change in growth parameters, and is most likely due to the change in In supply to the Au particle[6,9] as the NW grows longer than the diffusion length of In on the substrate. The NWs were subsequently transferred onto silicon substrates *via* drop-cast method to perform PL and magneto-PL studies on single NWs.

Figure 1a) shows a 45° tilted scanning electron microscopy (SEM) image taken on an ensemble of kinked NWs. The NWs have a fairly uniform morphology. The top segment, highlighted in red in the figure, is characterized by a WZ crystal phase, diameter of ~ 70 nm, hexagonal cross-section, and a growth direction along <0001> (WZ equivalent of ZB <111>). The bottom segment, highlighted in blue in the figure, has a ZB crystal phase with a rectangular cross-section (~ 120 nm on the long edge, ~ 90 nm on the short edge)[35], and grew along the [100]. Both segments of the NWs are almost non-tapered, and they are each ~1.4 μm long. Figure 1b) displays a transmission electron microscope (TEM) image of a single NW where the kinking angle is measured to be ~ 16°. The NWs have a very good crystal quality, with no twins in the ZB segment (except for one that initiates kinking) and very few stacking faults in the WZ segment. Twins and stacking faults are seen to form around a small region at the junction (green squares in figure 1b)) during simultaneous lateral over-growth. Further structural information on the junction is provided in the Supporting Information, SI, 1. The crystal quality of the NW is confirmed by high-resolution

TEM images in figures 1c) and d) for the ZB and WZ segments, respectively. The approximate regions of acquisition of figure 1c) and d) are marked by the blue and red boxes indicated by arrows in figure 1b), respectively. Finally, the attribution of ZB and WZ crystal phases is confirmed by the selected area diffraction patterns shown in the insets of figures 1c) and d).

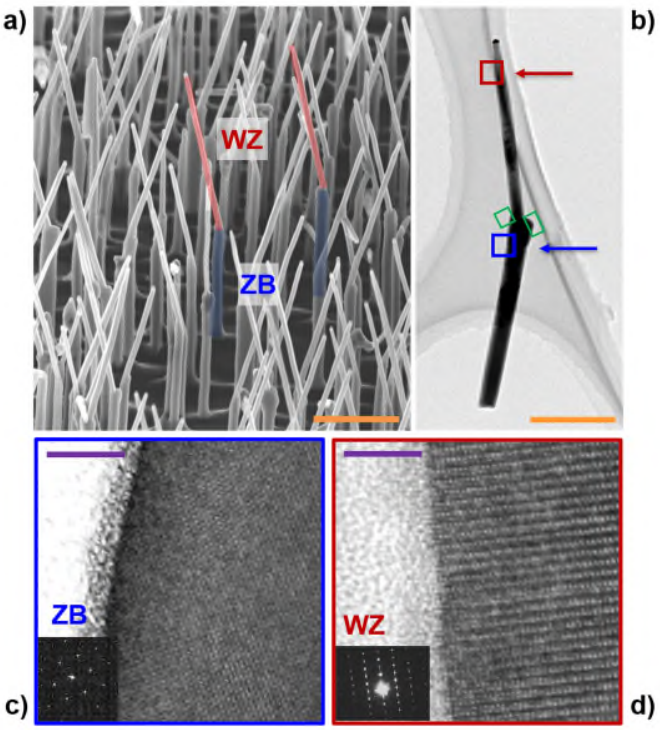

Figure 1. Electron microscopy characterization of kinked InP NWs. a) 45° tilted SEM image of an as-grown kinked NW ensemble. The regions highlighted in red and blue denote the WZ and ZB segments of the NW, respectively. b) TEM image of a NW showing the kink of ~ 16°. The blue and red boxes (see arrows) mark the regions where the high-resolution TEM images in panels c) and d), respectively, are obtained. Green squares mark the regions in which defective lateral growth occurs. c),d) Higher magnification images from the indicated ZB and WZ regions, respectively. These images show the good crystal quality of the NWs. Insets in c) and d) are the selected area diffraction patterns, confirming the ZB and WZ crystal phase of the different segments. Orange (panels a) and b)) and violet (panels c) and d)) scale bars are 500 and 5 nm, respectively.

Emission properties in absence of magnetic field. The bottom part of figure 2a) shows the μ-PL spectra obtained at temperature T = 5 K from the ZB and WZ segments of a single NW using a 50× objective at an excitation power density P_{exc}= 0.6 kW/cm^2. The PL spectrum from the WZ

region is characterized by an intense emission at 1.488 eV, attributed to the band-gap free excitons (FE) of the WZ crystal phase[30]. The PL spectrum collected from the ZB area is dominated by the FE emission that is at 1.412 eV[17,36]. A defect related broadband emission, which will be discussed in more detail related to Figure 2c) and in the magneto-PL measurements, is detected at energies below the FE.

For each of the segments, we have filtered the polarization of the PL signal parallel and perpendicular to the NW long-symmetry axis (see black and purple spectra in the bottom part of panel a)), the direction of which changes due to the kink. The PL emission was collected with a fixed and linear laser polarization, such that the relative orientations between laser polarization and each crystal axis remains the same during the experiments. The resulting degrees of linear polarization (ρ, calculated with the equation shown in the figure) for the two cases are shown in the top part of figure 2a) by open circles. It is clearly visible that the PL emission in the energy region of the WZ section (1.45-1.52 eV) is polarized perpendicular to the $\hat{c}$ axis, reaching a maximum value of ρ=0.5. The degree of polarization is positive, meaning the PL intensity polarized perpendicular to the WZ NW axis is larger than the one parallel to it. This is a consequence of the dipole selection rule in which band-gap transitions are only allowed for light polarization vector $\varepsilon \perp \hat{c}$ in WZ crystals[37]. On the other hand, the emission from the ZB segment (1.38-1.42 eV) shows an opposite degree of linear polarization (ρ=-0.25) reaching a maximum value smaller than that of the WZ segment. Indeed, in ZB crystals, specific electronic selection rules do not exist (the heavy and light holes being degenerate). However, the elongated shape and dimension of the NW yield an antenna effect[38], which tends to make PL emission polarized along the NW axis[13,39]. This antenna effect is also present in the WZ section, and, along with the finite numerical aperture (NA) of the microscope objective, is usually responsible for ρ being less than

1[39]. It should be noted that while the antenna effect in the absorption[40] and emission[41] of polarized light was calculated in NWs, its interplay with the WZ selection rules in still unclear.

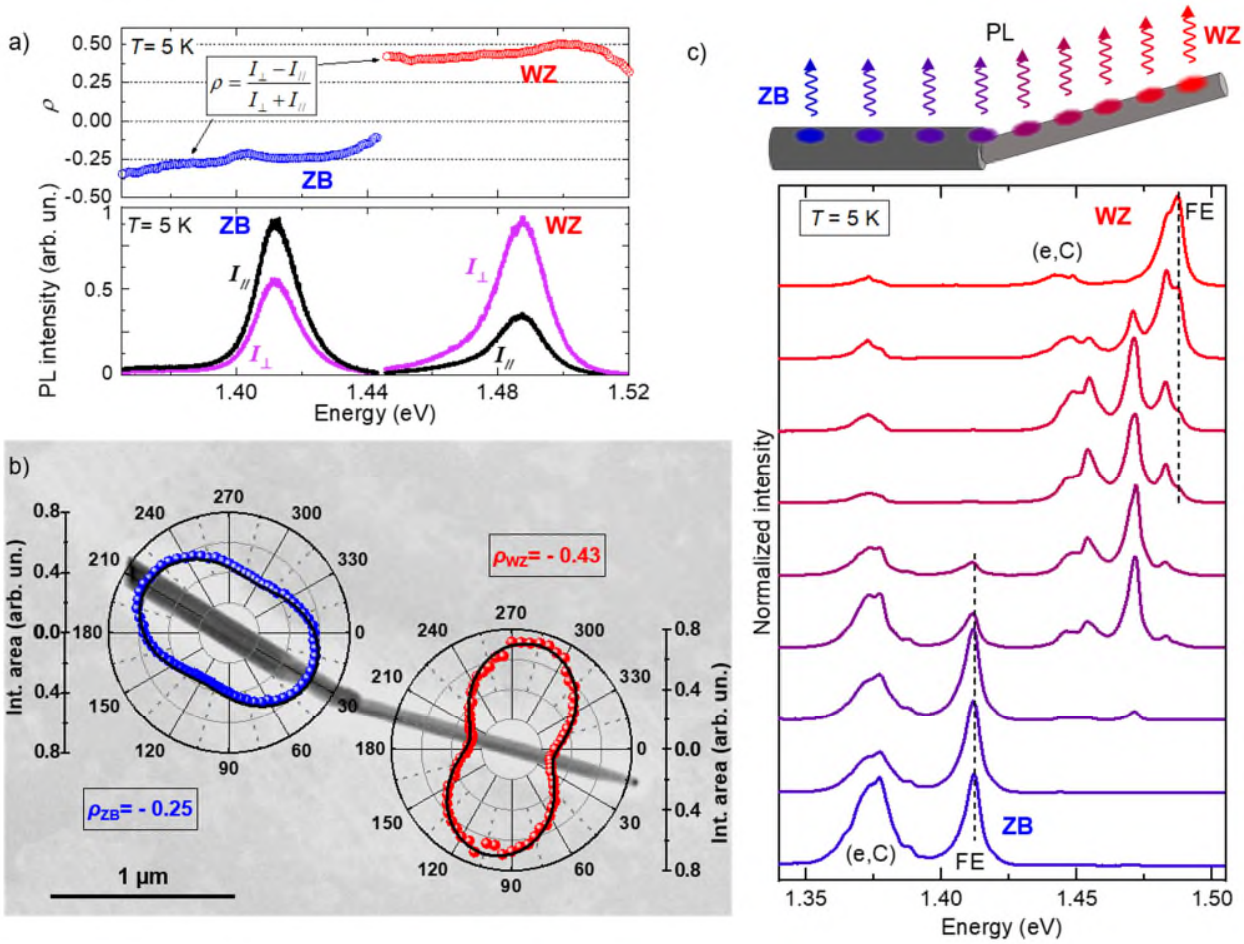

Figure 2. a) Bottom: PL spectra recorded at *T*=5 K from a single kinked InP NW (on the ZB and WZ segments, separately). The PL emission polarized parallel and perpendicular to the NW axis is indicated in black and purple, respectively. Spectra are normalized to the most intense spectrum for each NW segment. The parallel and perpendicular configurations for each NW segment were determined based on the polar plots shown in b). Top: open circles represent the degree of linear polarization, ρ, obtained by the indicated equation, applied to the PL spectra in the bottom panel. b) Corresponding SEM image of the NW investigated in a) superimposed with the corresponding polar plots for WZ (red) and ZB (blue) PL emissions. c) Spatially-resolved µ-PL measurements at *T*=5 K recorded at the indicated points along a typical kinked InP NW (see respectively colored circles in the top inset sketch). The sketch is just a schematic, and the laser spot is actually circular and the NW completely lying on the substrate. Each PL spectrum was normalized to its maximum. Dashed lines mark the energy of the ZB and WZ FEs.

The dependence of the emitted light on the angle θ between the polarizer axis and the pertinent NW long-symmetry axis can be derived by the Malus' law, and is equal to:

$$I(\theta) = \frac{1+\rho}{2}\cos^2(\theta - \theta_0) + \frac{1-\rho}{2}\sin^2(\theta - \theta_0), (1)$$

where θ_0 is an offset angle. This dependence has been experimentally determined by rotating the polarizer axis from 0 to 360° in steps of 5°. Then the PL intensity was integrated over 10 meV around the maximum peak in each ZB and WZ spectrum. In figure 2b), the resulting polar plots are superimposed on the SEM image of the same NW. It is clearly noticeable that in the WZ section light is polarized perpendicular to the NW axis, whereas in the ZB section light is polarized along the NW axis. Both results, expected in WZ and ZB NWs, suggest that the WZ and ZB segments have a good crystal quality, as a considerable number of staking faults might instead increase the disorder and decrease the degree of polarization. Moreover, reproducing the data using Eq. (1) and considering that the WZ intensity should be maximum at an angle of 90° with respect to the WZ $\hat{c}$ axis, we can exploit the polar plots to calculate the angle between the ZB and the WZ segments. A value of 16° is ascertained. This value is in very good agreement with the angle that is measured directly using the microscopy images (~ 16°) and that theoretically calculated using angles between crystal planes (15.8°)[9]. This study demonstrates that careful, all-optical measurements, can provide accurate structural information on axial crystal-phase homo-structured NWs and even circumvent electron microscopy measurements which could damage the NWs and subsequently affect their optical quality.

We also investigated the spatial dependence of the μ-PL spectrum along an entire single NW. Figure 2c) shows μ-PL spectra recorded at T = 5 K with P_{exc}= 0.031 kW/cm^2 at nine different positions (see the correspondence between positions and colors of the spectra) in the same backscattering geometry of Figure 2a) and b) but without filtering the polarization of the emitted

light. In the ZB region, we observe the FE transition at ~1.412 eV and an impurity-related band, mostly composed by the transition from free-electrons to neutral-carbon acceptors, (e,C), at ~ 1.375 eV[42]. In the WZ region, we observe the FE transition at 1.488 eV, a number of defect-related bands at energies 1.455 <*E*< 1.485 eV typical of WZ InP (see, *e.g.*, bands labelled as Z, Y, and V in ref. 20), and the (e,C) transition at ~ 1.45 eV. A weak emission from the ZB region is slightly visible in the spectra being collected from the WZ segment, and vice-versa. This might be due to the diameter of the laser spot and/or to carrier diffusion. We do not observe any specific transitions related to the kinked region. Instead, a decrease in the relative intensity between the high-energy bands (FE and nearby bands) and the defect/impurity bands is observed. Due to the relatively large laser spot compared to the size of the junction, this effect could even be explained by a lower effective power density on the two pure phases when measurements are made at the junction, as discussed in the description of the μ-PL map carried out at lower power (Figure S2) and of the power-dependence study (Figure S3), both shown in the SI2.

Emission properties under magnetic field. Magneto-PL measurements on single NWs were carried out at two temperatures, *T*=77 and 290 K, in order to highlight the dependence of different optical transitions on the magnetic field $\vec{B}$. The field $\vec{B}$ is directed perpendicular to the growth axes of both ZB and WZ segments, as the individual NWs are lying on the silicon substrate which they have been transferred to. The experimental geometry is sketched in the top inset of Figure 3 (for simplicity, we represent only the WZ segment of the NW, and therefore label the growth axis direction as ĉ). The laser wavevector ($\vec{k}_{\mathrm{L}}$) and PL wavevector ($\vec{k}_{\mathrm{PL}}$) were antiparallel to each other and both directed perpendicular to the NW growth axes. This configuration ($\vec{B} \parallel \vec{k}_{\mathrm{PL}} \perp \hat{c}$) is designated as the *Faraday* configuration. Carriers' motion occurs in planes perpendicular to $\vec{B}$ (one of such planes is represented in grey in the sketch), which means that in this configuration we

can measure the mass of carriers moving on these planes. We point out that henceforth, WZ carrier mass values will thus refer to the motion of carriers in a plane containing the ĉ axis of the WZ segment (see the orbit of electrons and holes in Figure 3). This motion corresponds to a convolution of carrier motion in a direction parallel and perpendicular to the WZ $\hat{c}$ axis, following the definitions reported in ref. 30. No circular polarization dependence of PL was observed at a high magnetic field (B=20 T, not shown here) at both measurement temperatures. Indeed, as shown in ref. 43, circular polarization is not expected if $\vec{B} \perp$ ĉ, independent of the orientation of $\vec{k}_{\mathrm{PL}}$ with respect to ĉ.

Figure 3a) displays the evolution of the PL spectra from an entire kinked NW with the field intensity varied from 0 to 29 T at T=77 K. The peak at 1.486 eV is due to FE transitions of the WZ region, while the FE transitions from the ZB region exhibit a more intense emission at 1.411 eV. There is also the (e,C) transition at energies ~ 40 meV lower than that of the ZB FE[42]. Finally, a weak peak at 1.34 eV, ascribable to a defect state, can be observed. For these measurements, the NW is excited with the laser spot at the center of the NW so that PL from both regions can be collected simultaneously.

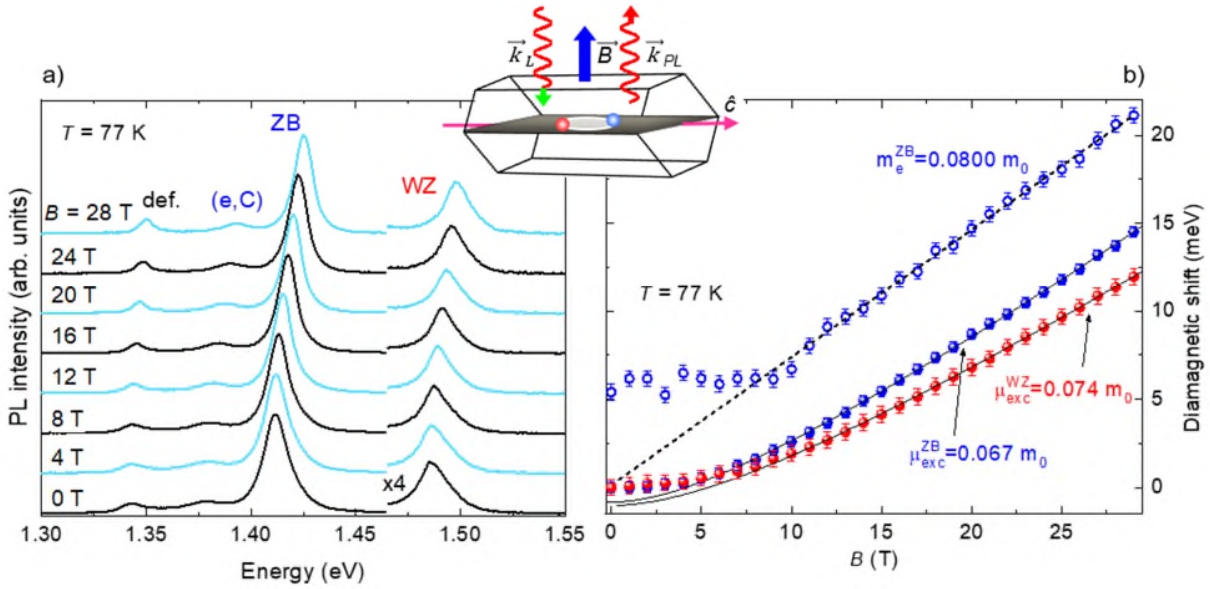

Figure 3. a) Selected PL spectra collected at T=77 K, P_{exc}=1 kW/cm^2, from a single NW with B varying from 0 to 29 T in the Faraday configuration $\vec{B} \parallel \vec{k}_{PL} \perp \hat{c}$ (sketched in the top inset). Each spectrum is separately normalized to its maximum, and shifted for clarity. The WZ data are multiplied by a factor of 4. The ZB and WZ free-exciton transitions are labeled as 'ZB' and 'WZ', the (e,C) transition is related to the ZB region and the 'def.' peak is probably due to recombination at a defect state. b) Diamagnetic shift of the ZB FE (blue filled dots), WZ FE (red filled dots), and ZB (e,C) (blue open circles) transitions as a function of B. The ZB (e,C) data are shifted up by 5 meV for clarity. The black lines are the fit to the data using the Cabib model for FE, from which the reported exciton reduced masses μ_{exc} are obtained. The dashed black line is a linear fit to the ZB (e,C) data using the Landau model for impurity transition from which the reported ZB electron mass m_e is obtained. Error bars in the experimental data were estimated based on the spectral resolution of the setup, the signal to noise ratio of the spectra, and the ensuing capability to determine the PL peak energy.

Figure 3b) shows the diamagnetic shift of the three transitions of interest as a function of B. The blue and red filled dots refer to the diamagnetic shift of FE in ZB and WZ segments, respectively, while the open blue circles denote the diamagnetic shift of (e,C) transition in the ZB segment (up-shifted by 5 meV). As discussed in detail in ref. 30, the (e,C) and the FE transitions display very different behaviors with the magnetic field. The (e,C) transition is not subjected to a large Coulomb potential whereas the FE is. This results in a linear dependence of the (e,C) transition with B, corresponding to the electron Landau level, and in a non-linear dependence of the FE, which is

due to the interplay between the magnetic field effect and the sizable Coulomb interaction acting on the charge carrier dynamics with comparable strength[20].

Let us first discuss the result obtained for the (e,C) transition in the ZB. There is no variation in the energy of the transition up to *B*=8 T and it increases linearly thereafter for higher fields. The observed plateau in the diamagnetic shift below a critical field value is due to the presence of scattering mechanisms that impede the termination of the cyclotron orbit and thus the establishment of the Landau levels[44]. The dashed black line displayed in figure 3b) is a linear fit to the data according to the Landau model with slope $\beta = \frac{e\hbar}{2m_e}$ providing an electron mass for ZB InP NWs $m^e = 0.0800 \pm 0.0005\, m_0$. This quantity has not been measured in NWs before. The closest comparison that can be made is with bulk [100] ZB InP at the same temperature of 77 K[45], though we are probing carrier motion in {110} planes in our NWs lying on the substrate (with {110} facet on top) and not in {100} planes as in bulk. The value found in NWs is in good agreement with the range of values of m^e= (0.0795-0.0815) m_0 estimated in ref. 45. This agreement can be reasonably expected since the current NWs are of good optical quality and their dimensions are large enough to neglect quantum confinement effects, conditions that allow us to probe the intrinsic properties of ZB (and WZ) InP.

In the case of the FE, both diamagnetic shifts show no significant changes below a critical field (B ~ 5 T) and then they increase following the perturbative Cabib model, which is appropriate to describe free excitons in magnetic field whenever the Coulomb interaction and the magnetic energy are comparable, as thoroughly discussed in refs. 20, 23, and 46. As for the (e,C), also in this case the occurrence of a critical field for the observation of sizable magnetic field effects is associated with scattering of free carriers with other carriers and ionized impurities[44]. The critical fields for the two FE transitions are lower than that of the (e,C) transition because the reduced

mass of FE is lighter than the effective electron mass, thus the cyclotronic frequency ω_c is greater and the condition $\omega_c\tau > 1$ is satisfied at lower magnetic fields[47]. The thin black lines are fits to the data according to the Cabib model, excluding the data below B = 6 T. The fact that the diamagnetic shift of the FE is well described with the Cabib model, which describes behavior of free-excitons, proves the excitonic nature of this transition, even at 77K. This is also confirmed by a lineshape analysis of the PL spectra of ZB and WZ InP NWs as a function of temperature, in absence of magnetic field, which shows that the excitonic contribution is higher than the band-to-band contribution.[17] The exciton reduced masses obtained from the fits are $\mu_{exc}^{WZ} = 0.074 \pm 0.004\, m_0$ and $\mu_{exc}^{ZB} = 0.067 \pm 0.001\, m_0$. The WZ mass is in good agreement with the known value of $\mu_{exc}^{WZ} = 0.072\, m_0$[30,46] within the error. The effective mass of the band gap FE of ZB InP has not been measured in NWs before. Our value is in good agreement with the value known for bulk [100] InP, $\mu_{exc}^{ZB} = 0.063$[46]. Given the similar value of the electron mass in the bulk and in our NWs, the difference in the exciton mass could be attributed mostly to a different hole mass, possibly arising from the different crystallographic orientation probed in NWs and bulk. This result suggests that, even in absence of quantum confinement, using the mass values of the bulk for ZB NWs can lead to some differences due to the NW facets being different to those typically probed in bulk, and that it is preferable to measure directly the properties of the NWs. Using the well-known relation between exciton, hole, and electron masses, $\frac{1}{\mu_{exc}} = \frac{1}{m^e} + \frac{1}{m^h}$, we have also determined the heavy/light hole mass in ZB NWs to be $m^h = 0.41 \pm 0.05\, m_0$. Overall, the measurement of the ZB and WZ FE mass highlights the heavier character of the exciton mass in WZ crystal than in ZB crystal in this geometry, in agreement with previous theoretical[27,34,48] and experimental[46] results. It is noted that to compare the experimental exciton reduced mass values with the ones extracted from theoretical works, the theoretical excitonic mass was derived from

$\frac{1}{\mu_{exc}} = \frac{1}{m^e} + \frac{1}{m^h}$, as only the electron and hole masses are given in the theoretical works; therein, m^h and m^e are calculated in the geometry of our experiment. In our experiments, we have $\vec{B} \parallel \vec{k}_{\mathrm{PL}} \perp \hat{c}$, therefore we are probing a combination, described by the cyclotron mass tensor, of carrier motion parallel and perpendicular to the WZ $\hat{c}$ axis. As a consequence, for the single carrier mass we have used the expression $m^{h,e} = \sqrt{m^{h,e,\parallel} m^{h,e,\perp}}$, where $m^{h,e,\parallel}$ and $m^{h,e,\perp}$ are the calculated hole and electron mass related to carrier motion parallel and perpendicular to $\hat{c}$, respectively[20,30].

Figure 4a) shows the μ-PL spectra recorded on a single NW at T = 290 K for increasing magnetic fields up to 27 T, in the energy range of the WZ emissions. Two optically allowed transitions can be observed: $\Gamma_7^{\mathrm{C}} \leftrightarrow \Gamma_9^{\mathrm{V}}$ (band A, namely the band-gap transition) and $\Gamma_7^{\mathrm{C}} \leftrightarrow \Gamma_{7u}^{\mathrm{V}}$ (band B, namely the transition from the bottom of the conduction band to the second valence band)[17]. Clearly, at this temperature, the signal coming from band B is more intense than that from band A. This is due to the presence of hot carriers, whose temperature can substantially exceed that of the lattice[49]. In these kinked NWs, the presence of hot carriers at room temperature is enabled by the relatively small diameter of the WZ segment. A temperature-dependent PL study (for B=0) from 150 K to room temperature of the WZ segments of these NWs is shown in SI3, where the carrier temperature determined by lineshape fits is also given (see the excitonic and band-to-band contributions in Figure S4). For a lattice temperature of 290 K, a carrier temperature of 427 K is determined, thus accounting for the large population of carriers in the second valence band that is involved in the B transition. In turn, this makes the present samples ideal for the investigation of the unknown magneto-optical properties of this transition in WZ NWs.

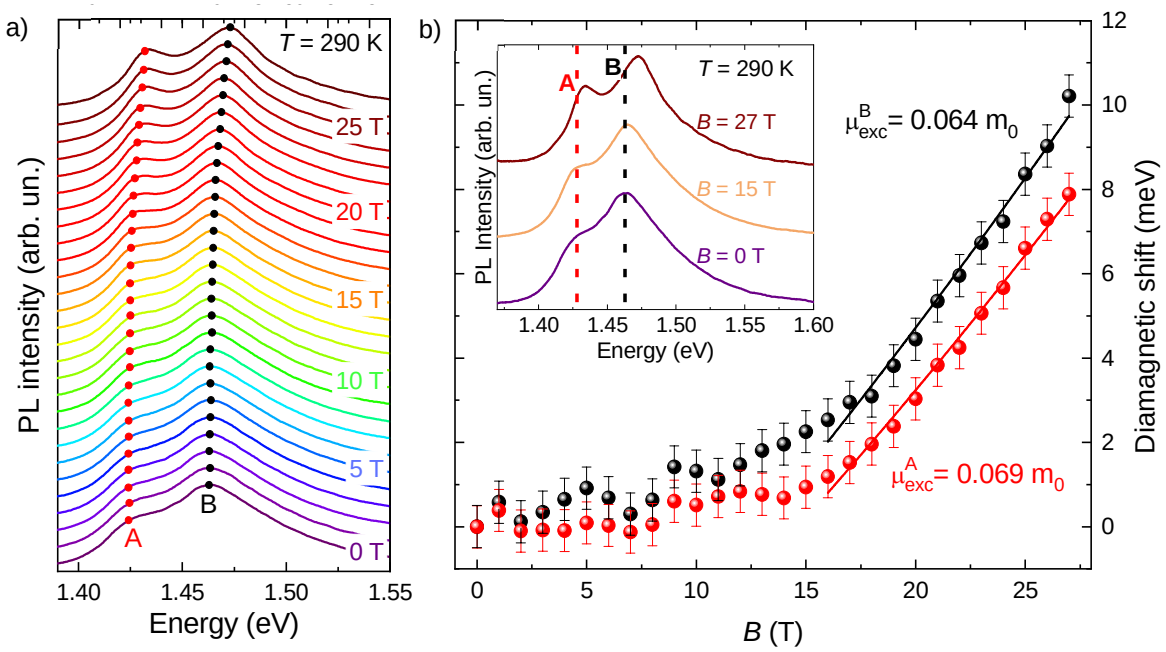

Figure 4. a) PL spectra collected at T=290 K, P_{exc}=4 kW/cm^2, from a single NW with B varying from 0 to 27 T in the Faraday configuration $\vec{B} \parallel \vec{k}_{PL} \perp \hat{c}$ depicted in Figure 3. The energy region of the WZ emission is displayed. Each spectrum is separately normalized to its maximum, and shifted for clarity. Transitions from the first (band A) and second (band B) optically allowed transitions are labeled. Full circles display the energy of the A and B free excitions as determined by the quantitative analysis described in the SI4. b) Diamagnetic shifts of the free excitons of the band A, red dots, and band B, black dots, as a function of B. Solid lines are the fits to the data using the Cabib model for FE, from which the reported exciton reduced masses are determined. The inset shows the PL spectra at B=0, 15, and 27 T. The dashed lines mark the approximate peak energies of bands A and B at zero magnetic field (not determined by the quantitative analysis). The different diamagnetic shift in peak energies of A and B bands is clearly seen, along with a line narrowing. Error bars were estimated in the same manner as in Figure 3b).

Despite the contribution from the band-to-band transitions to the PL lineshape at RT being higher than the excitonic contribution (see Figure S4 in SI3), we were able to quantitatively determine the energy of the free excitons (displayed as full circles in Figure 4a)) as a function of magnetic field by analysing the magneto-μ-PL spectra in Figure 4a) using the minima of the second derivative, as described in Figure S5 in SI4. Figure 4b) shows the resulting diamagnetic shifts of the free excitons associated to transitions A (red circles) and B (black circles). It can be noticed

that there is a very small, almost constant diamagnetic shift up to ~ 13 T, and then it increases for both the A and B bands. This is clearly visible in the inset, which shows the PL spectra at *B*=0, 15, and 27 T. Indeed, apart from a reduction of the linewidth due to the change of the density of states induced by the magnetic field[23], the two PL spectra at *B*=0 and 15 T are nearly identical, and the two peaks are almost at the same energy (see the dashed black and red lines drawn as a guides to the eyes). The increase of the critical field for the observation of sizable magnetic field effects with respect to that at *T*=77 K is likely due to the increase in the carrier scattering rate caused by higher lattice (and carrier) temperature.

The solid red and black lines in Figure 4b) are fits to the diamagnetic shift of the A and B transitions, according to the Cabib model, respectively. The data below 16 T are excluded from the fitting procedure. The FE reduced mass of the A excitons is $\mu_{exc}^{WZ,A} = 0.069 \pm 0.004\, m_0$ which is in good agreement with the one determined at *T*= 77 K in Figure 3 and previously reported values at low temperature[30,46]. A decrease with respect to the value at 77 K is likely due to a decrease in the electron mass with increasing temperature[45]. This testifies that we are able to reliably resolve the diamagnetic shift even at RT, despite the broad PL linewidths, which highlights the high quality of the NWs and demonstrates the need of very high magnetic fields to assess optical properties at high temperature. For the B transition, a lighter FE reduced mass is found, $\mu_{exc}^{WZ,B} = 0.064 \pm 0.004\, m_0$. This result is also confirmed by the larger diamagnetic shift of B transition at 27 T (~ 10 meV) in comparison to that of the A transition (~ 8 meV). Since the conduction band involved in transitions A and B is the same, the difference between the reduced masses of the A and B excitons is only ruled by the difference between the heavy and light hole masses of the WZ crystal structure, with only the first one being known. Using the electron mass value, which is known[30] (both theoretically and experimentally, and here we use the experimental

value, known only at 4.2 and 77 K) and the reduced mass of the exciton B above, we determine the light hole mass to be $m^{lh} = 0.26 \pm 0.05\, m_0$. This value is ~180 % smaller than the heavy hole mass at 77 K and ~140 % smaller than the heavy hole mass at RT (determined to be equal to $0.37 \pm 0.12\, m_0$ using the $\mu_{exc}^{WZ,A}$ derived in Figure 4b)). Moreover, it is in excellent agreement with the theoretical prediction of $0.247\, m_0$[34] which was based on DFT calculations performed in the same geometry as our experiment (namely, using the above discussed expression $m^h = \sqrt{m^{h,\parallel} m^{h,\perp}}$)[20,30]. Finally, it is worth pointing out that the experimental verification of calculated carrier masses is also useful in view of the investigation of gyromagnetic factors, whose calculations depend on the carrier masses[22], and is used in spin-based applications of NWs. The effective mass values determined in this and in previous works in ZB and WZ InP NWs are summarized in table 1.

InP NWs		Band-gap FE (m_0)		Light-hole FE (m_0)	Free electron (m_0)			Heavy hole (m_0)			Light hole (m_0)
	T (K)	$\mu_{exc,A}^{\parallel,\perp}$	$\mu_{exc,A}^{\perp}$	$\mu_{exc,B}^{\parallel,\perp}$	$m_e^{\parallel,\perp}$	$m_e^{\perp}$	$m_e^{\parallel}$	$m_{hh}^{\parallel,\perp}$	$m_{hh}^{\perp}$	$m_{hh}^{\parallel}$	$m_{lh}^{\parallel,\perp}$
WZ	4.2	0.071± 0.001^{+}	0.068± 0.001^{+}		0.085± 0.001^{+}	0.091± 0.002^{+}					
	77	0.074± 0.004; 0.072± 0.001;* 0.071± 0.001^{+}	0.067± 0.001^{+}; 0.068± 0.001*		0.085± 0.001^{+}	0.093± 0.001^{+}	0.078± 0.002^{+}	0.47± 0.02^{+}	0.25± 0.02^{+}	0.81± 0.18^{+}	
	RT	0.069± 0.004		0.064±0.004				0.37± 0.12			0.26±0.05
ZB	77	μ_{exc}=0.067±0.001			m_e=0.0800±0.0005			$m_{hh,lh}$=0.41±0.05			

Table 1. Summary of all the effective masses in InP NWs experimentally assessed at the indicated temperature in this work (no symbol) and in the literature ($^{+}$ref. 30; *ref. 46). Data for WZ NWs refer to the present kinked NWs or to NWs grown by selective area epitaxy[30] or vapor liquid solid[46], all grown along the ZB <111> equivalent, WZ <0001> ĉ axis; superscripts ∥ and ⊥ indicate the mass in a direction parallel and perpendicular to the WZ ĉ axis, respectively, and superscript ∥,⊥ indicates the convolution of the two motions. Data for ZB NWs refer to the kinked NWs of this work, grown along [100] (with a {110} NW side facet facing up and probed by the laser when the NW is lying on the substrate); carrier motion was probed in {110} planes.

Conclusions We investigated the optical and magneto-optical properties of single, crystal-phase homo-structured InP NWs. Optical characterization of the single NWs in absence of magnetic field provided valuable information about the optical selection rules of the WZ and ZB crystal structures. Using polarization-resolved μ-PL experiments, we determined the kinking angle of the homo-structured NWs, matching that obtained by electron microscopy. By applying a magnetic field perpendicular to the NW axis at 77 K, the value of the electron mass in ZB (which is related to the diamagnetic shift of its' impurity-related recombination), and the reduced masses of free excitons in both the ZB and WZ segments were obtained. Finally, magneto-μ-PL experiments performed also at room temperature on the WZ segment of a single NW allowed us to determine, for the first time, the value of the light hole mass of WZ InP. In conclusion, the full picture of the relevant effective masses (first and second band-gap free excitons, electrons in the first conduction band[30], and holes in the first[30] and second valence bands) in WZ InP are now known. For ZB InP, we measured the electron and hole mass and the mass of the band-gap free excitons in NWs, and found that for the electron mass the values known in the bulk also apply to NWs. The importance of a complete experimental knowledge of carrier and excitons effective masses is twofold: it can act as a benchmark for the calculations of the band structures of WZ and ZB InP, and is valuable for the design of InP NW optoelectronics, electronic, and thermoelectric devices.

Methods

Growth of nanowires and structural characterization. After depositing the colloidal Au particles, the InP (100) substrates were loaded to the reactor and annealed at 390 °C under PH_3 flow for 10 minutes, before ramping to the growth temperature of 475 °C. NW growth was initiated with a TMIn flow of 2.02×10^{-6} mol/min and a PH_3 flow corresponding to a V/III ratio of 350 to ensure a high yield of vertical [100] ZB segments[9]. After 15 minutes of growth, the V/III ratio was

reduced to 220 in order to minimize lateral growth. The spontaneous change in growth direction and phase has taken place approximately 90 min into the growth. Growth was carried out for a total of 180 min before switching off TMIn and cooling down under PH_3.

The morphological and structural analysis were carried out using a FEI Helios 600 NanoLab scanning electron microscope and a JEOL 2100F transmission electron microscope operating at 200 kV, respectively.

Optical and magneto-optical measurements. Zero magnetic-field photoluminescence measurements were performed at 5 K using a He closed-cycle cryostat. PL was excited by a frequency-doubled Nd:YVO_4 laser (532 nm) using a 50x objective (NA = 0.5), resulting in a spot diameter of ~ 1 μm. Micro-PL studies along the single NW (Figure 2c), and SI2) were performed with a 100x objective with NA = 0.75 (spot size ~ 0.75 μm). The collected PL was dispersed by a 0.75 m monochromator and detected by a liquid nitrogen-cooled Si CCD. In polarization studies, the polarization of the exciting laser was not varied, instead the emitted PL was filtered using a linear polarizer, preceded by a lambda-half plate, ensuring the light entering the spectrometer was always of the same polarization. For PL measurements under magnetic field, the samples were placed in a water-cooled Bitter magnet at T=77 or 290 K using a bath cryostat. The PL was excited by a frequency-doubled Nd:YVO_4 laser focused using a 20x objective (spot diameter ~ 1.5 μm), collected by the same objective, dispersed by a 0.30 m monochromator and detected by a liquid nitrogen-cooled Si CCD.

Supporting Information

Supporting Information is available in the online version of the paper. It contains further structural characterization of the nanowires, photoluminescence spectra as a function of power, temperature,

and position along the nanowires, and explanation of the method employed to extract the exciton energy in the PL spectra acquired at room temperature.

AUTHOR INFORMATION

Corresponding Authors

*marta.deluca@unibas.ch

*antonio.polimeni@roma1.infn.it

[#]Present address: Samsung Austin Semiconductors, 12100 Samsung Blvd, Austin, TX 78754, USA

Acknowledgements. MD acknowledges support from the Swiss National Science Foundation under the Ambizione grant (Grant No. PZ00P2_179801). We acknowledge the support of HFML-RU/FOM, member of the European Magnetic Field Laboratory (EMFL). Part of this work has been supported by EuroMagNET II under the EU contract number 228043. AGDA gratefully acknowledges the financial support of the Presidential Postdoctoral Fellowship program of the Nanyang Technological University. The Australian authors acknowledge the Australian Research Council, the Australian National Fabrication Facility (ANFF), ACT node and the Australian Microscopy and Microanalysis Research Facility (AMMRF), ACT node. E.B. and A.P. acknowledge funding from the Regione Lazio programme “Progetti di Gruppi di ricerca” legge Regionale n. 13/2008 (SINFONIA project, prot. n. 85-2017-15200) via LazioInnova spa. H.A.F. acknowledges funding from the EPSRC (Grant No: EP/P000916/1). The authors thank F. Mura

from CNIS (Sapienza University of Rome) for his contribution to SEM characterization of the nanowires.

REFERENCES

[1] Dick, K. A.; Thelander, C.; Samuelson, L.; and Caroff, P. Crystal Phase Engineering in Single InAs Nanowires. *Nano Lett.* **2010**, *10*, 3494-3499.

[2] Assali, S.; Lähnemann, J.; Vu, T. T. T.; Jöns, K. D.; Gagliano, L.; Verheijen, M. A.; Akopian, N.; Bakkers, E. P. A. M.; Haverkort, J. E. M. Crystal Phase Quantum Well Emission with Digital Control. *Nano Lett.* **2017**, *17*, 6062-6068.

[3] De Luca, M.; Fasolato, C.; Verheijen, M. A.; Ren, Y.; Swinkels, M. Y.; Koelling, S.; Bakkers, E. P. A. M.; Rurali, R.; Cartoixa, X.; Zardo, I. Phonon Engineering in Twinning Superlattice Nanowires. *Nano Lett.* **2019**, *19*, 74702-4711.

[4] Lehmann, S.; Wallentin, J.; Jacobsson, D.; Deppert, K.; Dick, K. A. A General Approach for Sharp Crystal Phase Switching in InAs, GaAs, InP, and GaP Nanowires Using Only Group V Flow. *Nano Lett.* **2013**, *13*, 9, 4099-4105.

[5] Shen, Y.; Lebedev, O. I.; Turner, S.; Van Tendeloo, G.; Song, X.; Yu, X.; Wang, Q.; Chen, H.; Dayeh, S. A.; and Wu, T. Size-Induced Switching of Nanowire Growth Direction: a New Approach Toward Kinked Nanostructures. *Adv. Funct. Materials*, **2016**, *26*, 3687-3695.

[6] Wang, J.; Plissard, S. R.; Verheijen, M. A.; Feiner, L.-F.; Cavalli, A.; and Bakkers, E. P. A. M. Reversible Switching of InP Nanowire Growth Direction by Catalyst Engineering. *Nano Lett.* **2013**, *13*, 3802-3806.

[7] B. Tian, T. Cohen-Karni, Q. Qing, X. Duan, P. Xie, C. M. Lieber. Three-dimensional, Flexible Nanoscale Field-Effect Transistors as Localized Bioprobes. *Science* **2010**, *329*, 830-834.

[8] J. F. Zimmerman, G. F. Murray, Y. Wang, J. M. Jumper, J. R. Austin, and B. Tian. Free-Standing Kinked Silicon Nanowires for Probing Inter- and Intracellular Force Dynamics. *Nano Lett.* **2015**, *15*, 5492-5498.

[9] Fonseka, H. A.; Caroff, P.; Wong-Leung, J.; Ameruddin, A. S.; Tan, H. H.; and Jagadish, C. Nanowires Grown on InP (100): Growth Directions, Facets, Crystal Structures, and Relative Yield Control. *ACS Nano* **2014,** *8*, 6945-6954.

[10] Fasolato, C.; De Luca, M.; Djomani, D.; Vincent, L.; Renard, C.; Di Iorio, G.; Paillard, V.; Amato, M.; Rurali, R.; and Zardo, I. Crystalline, Phononic, and Electronic Properties of Heterostructured Polytypic Ge Nanowires by Raman Spectroscopy. *Nano Lett.* **2018**, *18*, 7075.

[11] Bouwes Bavinck, M.; Jöns, K. D.; Zieliński, M.; Patriarche, G.; Harmand, J-C.; Akopian, N.; Zwiller, V. Photon Cascade from a Single Crystal Phase Nanowire Quantum Dot. *Nano Lett.* **2016**, *16*, 1081-1085.

[12] Chen, I-J.; Lehmann, S.; Nilsson, M.; Kivisaari, P.; Linke, H.; Dick, K. A.; Thelander, C. Conduction Band Offset and Polarization Effects in InAs Nanowire Polytype Junctions. *Nano Lett.* **2017**, *17*, 902-908.

[13] De Luca, M.; Lavenuta, G.; Polimeni, A.; Rubini, S.; Grillo, V.; Mura, F.; Miriametro, A.; Capizzi, M.; Martelli, F. Excitonic Recombination and Absorption in InGaAs/GaAs Heterostructure Nanowires. *Phys. Rev. B* **2013**, *87*, 235304.

[14] Senichev, A.; Corfdir, P.; Brandt, O.; Ramsteiner, M.; Breuer, S.; Schilling, J.; Geelhaar, L.; Werner, P. Electronic Properties of Wurtzite GaAs: A Correlated Structural, Optical, and Theoretical Analysis of the Same Polytypic GaAs Nanowire. *Nano Res.* **2018**, *11*, *4708*.

[15] Greil, J.; Assali, A.; Isono Y.; Belabbes, A.; Bechstedt, F.; Valega Mackenzie F. O.: Yu. Silov, A.; Bakkers, E. P. A. M.; Haverkort, J. E. M. Optical Properties of Strained Wurtzite Gallium Phosphide Nanowires. *Nano Lett.* **2016**, *16*, 3703-3709.

[16] da Silva, B.C.; Couto, O.D.D.; Obata, H.T.; de Lima, M. M.; Bonani, F. D.; de Oliveira, C. E.; Sipahi, G. M.; Iikawa, F.; and Cotta, M. A. Optical Absorption Exhibits Pseudo-Direct Band Gap of Wurtzite Gallium Phosphide. *Sci. Rep.* **2020**, *10*, 7904.

[17] Zilli, A.; De Luca, M.; Tedeschi, D.; Fonseka, H. A.; Miriametro, A.; Tan, H. H.; Jagadish, C.; Capizzi, M.; Polimeni, A. Temperature Dependence of Interband Transitions in Wurtzite InP Nanowires. *ACS Nano* **2015**, *9*, 4277-4287.

[18] Rota, M. B.; Ameruddin, A. S.; Fonseka, H. A.; Gao, Q.; Mura, F.; Polimeni, A.; Miriametro, A.; Tan, H. H.; Jagadish, C.; and Capizzi, M. Bandgap Energy of Wurtzite InAs Nanowires. *Nano Lett.* **2016** *16*, 5197-5203.

[19] Knutsson, J. V.; Lehmann, S.; Hjort, M.; Lundgren, E.; Dick, K. A.; Timm, R.; and Mikkelsen, A. Electronic Structure Changes Due to Crystal Phase Switching at the Atomic Scale Limit. *ACS Nano* **2017**, *11*, 10519-10528.

[20] De Luca, M.; and Polimeni, A. Electronic Properties of Wurtzite-Phase InP Nanowires Determined by Optical and Magneto-Optical Spectroscopy. *Appl. Phys. Rev.* **2017**, *4*, 041102.

[21] Corfdir, P.; Van Hattem, B.; Uccelli, E.; Conesa-Boj, S.; Lefebvre, P.; Fontcuberta i Morral, A.; Phillips, R. T. Three-Dimensional Magneto-Photoluminescence as a Probe of the Electronic Properties of Crystal-Phase Quantum Disks in GaAs Nanowires. *Nano Lett.* **2013**, *13*, 5303-5310.

[22] Tedeschi, D.; De Luca, M.; Faria Junior, P. E.; Granados del Águila, A.; Gao, Q.; Tan, H. H.; Scharf, B.; Christianen, P. C. M.; Jagadish, C.; Fabian, J.; and Polimeni A. Unusual Spin Properties Of Inp Wurtzite Nanowires Revealed By Zeeman Splitting Spectroscopy. *Phys. Rev. B* **2019**, *99*, 161204(R).

[23] De Luca, M.; Rubini, S.; Felici, M.; Meaney, A. J.; Christianen, P. C. M.; Martelli, F.; and Polimeni, A. Addressing the Fundamental Electronic Properties of Wurtzite GaAs Nanowires by High-Field Magneto-Photoluminescence Spectroscopy. *Nano Lett.* **2017**, *17*, 6540-6547.

[24] Faria Junior, P. E.; Tedeschi, D.; De Luca, M.; Scharf, B.; Polimeni, A.; and Fabian, J. Common Nonlinear Features and Spin-Orbit Coupling Effects in the Zeeman Splitting of Novel Wurtzite Materials. *Phys. Rev. B* **2019**, *99*, 195205.

[25] Płachta J, Kaleta A, Kret S, Kazimierczuk T, Połczyńska K, Kossacki P, Karczewski G, Wojtowicz T, Kossut J, Wojnar P., Polarization and Magneto-Optical Properties of Excitonic Emission From Wurtzite CdTe/(Cd,Mg)Te Core/Shell Nanowires. *Nanotechnology* **2020**, *31*, 215710.

[26] S. Furthmeier, F. Dirnberger, M. Gmitra, A. Bayer, M. Forsch, J. Hubmann, C. Schüller, E. Reiger, J. Fabian, T. Korn, and D. Bougeard, *Nature Commun.* **2016**, *7*, 12413

[27] De, A.; and Pryor, C. E. Predicted Band Structures of III-V Semiconductors in the Wurtzite Phase. *Phys. Rev. B* **2010**, *81*, 155210.

[28] Kirchartz, T.; and Rau, U. Linking Structural Properties with Functionality in Solar Cell Materials – the Effective Mass and Effective Density of States. *Sustain. Energ. Fuels* **2018**, *2*, 1550-1560.

[29] Wallentin, J. ; Anttu, N.; Asoli, D.; Huffman, M.; Åberg, I. ; Magnusson, M. H.; Siefer, G.; Fuss-Kailuweit, P.; Dimroth, F.; Witzigmann, B.; Xu, H. Q.; Samuelson, L.; Deppert, K.; Borgström, M. T. InP Nanowire Array Solar Cells Achieving 13.8% Efficiency by Exceeding the Ray Optics Limit. *Science* **2013**, 339, 1057-1060.

[30] Tedeschi, D.; De Luca, M.; Granados del Aguila, A.; Gao, Q.; Ambrosio, G.; Capizzi, M.; et al. Value and Anisotropy of the Electron and Hole Mass in Pure Wurtzite InP Nanowires, *Nano Lett.* **2016,** *16, 6213-6221*.

[31] S. Perera, T. Shi, M.A. Fickenscher, H.E. Jackson, L.M. Smith, J. Yarrison-Rice, S. Paiman, Q. Gao, H.H. Tan, and C. Jagadish. Illuminating the Second Conduction Band and Spin-orbit Energy in Single Wurtzite InP Nanowires. *Nano Lett.* **2013**, *13*, 5367.

[32] De Luca, M.; Polimeni, A.; Capizzi, M.; Meaney, A. J.; Christianen, P. C. M.; Maan, J. K.; Mura, F.; Rubini, S.; Martelli, F. Determination of Exciton Reduced Mass and Gyromagnetic Factor of Wurtzite (InGa)As Nanowires by Photoluminescence Spectroscopy under High Magnetic Fields. *ACS Nano* **2013**, *7*, 10717-10725.

[33] Wang, X.; Zardo, I.; Spirkoska, D.; Yazji, S.; Ng, K. W.; Ko, W.; Chang-Hasnain, C.; Finley, J.; Abstreiter, G. Valence Band Splitting in Wurtzite InGaAs Nanoneedles Studied by Photoluminescence Excitation Spectroscopy. *ACS Nano* **2014**, *8*, 11440.

[34] Junior, P. E. F.; Campos, T.; Bastos, C. M.; Gmitra, M.; Fabian, J.; and Sipahi, G. M. Realistic Multiband k·p Approach from Ab Initio and Spin-orbit Coupling Effects of InAs and InP in Wurtzite Phase. *Phys. Rev. B* **2016**, *93*, 235204.

[35] Fonseka, H. A.; Caroff, P.; Guo, Y.; Sanchez, A. M.; Tan, H. H.; and Jagadish C. Engineering the Side Facets of Vertical [100] Oriented InP Nanowires for Novel Radial Heterostructures. *Nanoscale Research Lett.* **2019**, *14*, 399, 1-10.

[36] E. Kubota, Y. Ohmori, and K. Sugii. Electrical and Optical Properties of Mg-, Ca-, and Zn-doped InP Crystals Grown by the Synthesis, Solute Diffusion Technique. *J. Appl. Phys.* **1984**, *55*, 3779-3784.

[37] Tronc, P.; Kitaev, Yu. E.; Wang, G.; Limonov, M. F.; Panfilov, A. G.; Neu, G. Optical Selection Rules for Hexagonal GaN. *phys. stat. sol. B* **1999**, *216*, 599-603.

[38] Fang, L.; Zhao, X.; Chiu, Y.-H.; Ko, D.; Kongara, M. R.; Lemberger, T. R.; Padture, N. P.; Yang, F.; Johnston-Halperin, E. Comprehensive Control of Optical Polarization Anisotropy in Semiconducting Nanowires. *Appl. Phys. Lett*. **2011**, *99*, 141101.

[39] De Luca, M.; Zilli, A.; Fonseka, H. A.; Mokkapati, S.; Miriametro, A.; Tan, H. T.; Smith, L. M.; Jagadish, C.; Capizzi, M.; Polimeni, A. Polarized Light Absorption in Wurtzite InP Nanowire Ensembles. *Nano Lett.* **2015**, *15*, 998-1005.

[40] Swinkels, M. Y.; Campo, A.; Vakulov, D.; Kim, W.; Gagliano, L.; Steinvall, S. E.; Detz, H.; De Luca, M.; Lugstein, A.; Bakkers, E.; Fontcuberta i Morral, A.; Zardo, I. Measuring the optical absorption of single nanowires. *Phys. Rev. Appl.* **2020** (in press).

[41] Grzela, G; Paniagua-Domínguez, R.; Barten, T.; Fontana, Y; Sánchez-Gil, J. A.; Gómez Rivas, J. Nanowire Antenna Emission. *Nano Lett.* **2012**, *12*, 5481-5486.

[42] Zhu, L. D., Chan, K. T., Wagner, D. K., & Ballantyne, J. M. Photoluminescence Study of the Growth of Indium Phosphide by Metalorganic Chemical Vapor Deposition. *J. Appl. Phys.* **1985**, *57*, 5486-8.

[43] Rodina, A. V.; Dietrich, M.; Göldner, A.; Eckey, L.; Hoffmann, A.; Efros, Al. L; Rosen, M.; Meyer, B. K. Free Excitons in Wurtzite GaN. *Phys. Rev. B* **2001**, *64*, 115204.

[44] Pettinari, G.; Polimeni, A.; Blokland, J. H.; Trotta, R.; Christianen, P. C. M.; Capizzi, M.; Maan, J. C.; Lu, X.; Young, E. C. Compositional Dependence of the Exciton Reduced Mass in $GaAs_{1-x}Bi_x$ (x= 0-10%). *Phys. Rev. B*, **2010**, *81*, *235211*.

[45] Schneider, D.; Rürup, D.; Schönfelder, B.; Schlachetzki, A. Effective Mass and Energy-band Parameters in InP by Magnetophonon Effect. Zeitschrift für Physik B Condensed Matter, 1996, 100, 33-38.

[46] De Luca, M.; Polimeni, A.; Fonseka, H. A.; Meaney, A. J.; Christianen, P. C. M.; Maan, J. C.; Paiman, S.; Tan, H. H.; Mura, F.; Jagadish, C.; Capizzi, M. Magneto-optical Properties of Wurtzite-phase InP Nanowires. *Nano Lett.* **2014**, *14*, 4250-4256.

[47] Pettinari, G.; Capizzi, M.; and Polimeni, A. Carrier Masses and Band-gap Temperature Sensitivity in Ga(AsBi) Alloys. *Semic. Sci. and Technol.* **2015**, *30*, 094002, 1-9.

[48] F. Bechstedt and A. Belabbes. Structure, Energetics, and Electronic States of III-V Compound Polytypes. *J. of Phys.: Cond. Matt.* **2013**, *25*, 273201.

[49] Tedeschi, D.; De Luca, M.; Fonseka, H. A.; Gao, Q.; Mura, F.; Tan, H. H.; Rubini, S.; Martelli, F.; Jagadish, C.; Capizzi, M.; Polimeni, A. Long-lived Hot Carriers in III-V Nanowires. *Nano Lett.* **2016,** *16, 3085-309.*